Design and Hysteresis Modeling of a Miniaturized Elastomer-Based Clutched Torque Sensor

Ning Sun, Long Cheng, *Senior Member, IEEE*, and Xiuze Xia

***Abstract*— Elastic torque sensors have been widely used for small-scale robots such as hand exoskeletons to achieve torque control. However, designing a miniaturized and lightweight elastic torque sensor with human–machine interaction safety is still a challenge. In this article, a novel miniaturized and lightweight elastomer-based clutched torque sensor is presented. A rubber spring is designed and used to reduce its volume and weight. A wafer disk clutch is devised to improve mechanical safety. The torque sensor is 29.5 mm × 18 mm × 24 mm in dimension and weighs 23 g. Compared with the state-of-the-art elastic torque sensors for hand exoskeletons, the volume-to-torque ratio is reduced by 15.48%, and its weight is reduced by 23.33%. Since the hysteresis characteristics of the rubber spring leads to a nonlinear deformation–torque relationship, an improved parametric Gaussian process regression (PGPR) method based on the nonlinear autoregressive moving average structure with exogenous inputs (NARMAX) is proposed. A combined kernel function for the improved PGPR is designed to improve the fitting performance. Finally, experiments have been conducted to verify the mechanical safety and torque sensing performance. The force caused by collision on the proposed torque sensor is less than that on the torque sensor without the clutch (reduced by 51.78%). The proposed hysteresis model can reduce the maximum absolute modeling error to 7% compared with those of other intelligent hysteresis models (the modeling error is 12.32%). Therefore, the experimental results indicate that the proposed torque sensor can improve the mechanical safety and achieve accurate torque sensing.**

***Index Terms*— Clutch, elastic torque sensor, hysteresis modeling, mechanical design, rubber spring.**

I. Introduction

WEARABLE robots, such as hand exoskeleton robots, have been widely developed and studied for neuro-motor rehabilitation [1], [2]. Research has indicated that force-control-based strategies are more conducive for the rehabilitation of limbs [3]. To achieve force control, human–machine interaction torques or forces need to be measured by the piezoresistive sensors or the strain beams using the deformation of sensitive elements [4], [5]. However, these devices are difficult to use in actual applications due to undesired contact conditions or small strain that is difficult to measure. Recently, elastic torque sensor has attracted attention from the torque/force measurement community. An elastic element is connected in series between the motor and the output end, and its application can solve the contact problem and enlarge deformation [6]. Torque or force can be estimated by measuring the deformation of the elastic element. Moreover, the elastic element provides inherent mechanical compliance, and it is promising in the robotic systems that physically interact with a human being [7]. However, there are still numerous design challenges for the elastic torque sensors applied for hand exoskeletons because of the limitations in terms of size, lightness, and human–machine interaction safety [8]–[10].

Various miniaturized and lightweight elastic torque sensors (also known as series elastic actuators in some references) have been designed and applied for hand exoskeleton robots. Generally, the elastic elements in these sensors use metal springs, such as compression spring, helical torsion (HT) spring, and structural spring. For example, Baldoni *et al.* [8] and Marconi *et al.* [11] designed two different miniaturized elastic torque sensors: cam-compression-spring-based sensor and tangential-compression-spring-based sensor. Jo and Bae [12] proposed a unidirectional force sensor with a linear compressed spring for a hand exoskeleton robot. Guo *et al.* [13] designed a linear force sensor with a wave disk spring. Agarwal *et al.* [14] and Yun *et al.* [15] proposed a Bowden-cable-based compression spring torque sensor (LC-sensor) for an index finger exoskeleton. Furthermore, the Bowden-cable-based torque sensor using two helical torsion springs (HT-sensor) has been developed and tested [9]. Zhang *et al.* [6] also presented a Bowden-cable-based compression spring torque sensor with application to a thumb finger exoskeleton. Refour *et al.* [16] designed a bidirectional torque sensor with two linear compressed springs placed against each other. Bianchi *et al.* [17] designed an elastic torque sensor with a structural spring through the innovative topology optimization method. However, the weight-to-stiffness and volume-to-stiffness ratios of these sensors are high because of the large size of metal springs. The rubber springs are of low weights and volumes, so the weight-to-stiffness and volume-to-stiffness ratios of the torque sensors with the rubber springs are much more desirable [18]. Moreover, rubber springs have inherent damping to reduce

Manuscript received October 28, 2021; revised December 7, 2021; accepted February 1, 2022. Date of publication February 16, 2022; date of current version March 9, 2022. This work was supported in part by the Beijing Municipal Natural Science Foundation under Grant JQ19020 and in part by the National Natural Science Foundation of China under Grant 62025307 and Grant U1913209. The Associate Editor coordinating the review process was Peter X. Liu. *(Corresponding author: Long Cheng.)*

The authors are with the State Key Laboratory of Management and Control for Complex Systems, Institute of Automation, Chinese Academy of Sciences, Beijing 100190, China, and also with the School of Artificial Intelligence, University of Chinese Academy of Sciences, Beijing 100049, China (e-mail: long.cheng@ia.ac.cn).

Digital Object Identifier 10.1109/TIM.2022.3152307

undesired oscillatory motion [19]. Therefore, how to design an elastic torque sensor using rubber springs instead of metal springs for hand exoskeleton robots needs to be further explored. In addition, it is worth noting that the rubber springs exhibit hysteresis nonlinearities, which makes torque sensing complicated [20].

To achieve accurate torque sensing, it is necessary to have a well-defined sensor model. Generally, the existing hysteresis models can be classified into two categories: physics-based models and data-based phenomenological models. The physics-based models include Hooke's law [21], [22], Maxwell model [23], Kelvin–Voigt model [23], standard linear solid model [24], and Burgers model [25]. These models may lack an explicit expression of hysteresis nonlinearity. In contrast, the data-based phenomenological models can better describe the hysteresis characteristics because they treat hysteresis nonlinearity by a clearly structured model. The data-based phenomenological models for rubber spring are mainly traditional parametric hysteresis models, such as exponential loading model (ELM) [26], polynomial model [27], nonlinear backlash model (NBM) [28], improved NBM [18], and improved Prandtl–Ishlinskii (PI) model [19]. The above methods consider either the amplitude characteristics or the frequency characteristics of the training data to establish the hysteresis models. However, both the amplitude and frequency characteristics have an influence on the hysteresis characteristics, which should be considered simultaneously [18], [19].

Some machine learning methods are introduced to model hysteresis nonlinearity since they have a strong capability of modeling nonlinear systems. For example, based on the nonlinear autoregressive moving average model with exogenous inputs (NARMAX), Cheng *et al.* [29] designed a neural network (NN) model to model piezoelectric actuator's hysteresis, and they also proposed a long short-term memory (LSTM) NN to model pneumatic artificial muscle's hysteresis [30]. However, these models are designed for specific applications and lack a guided way to determine the components of the model. As an alternative, kernel-based methods, such as Gaussian processes (GPs), can be used because of their flexibility [31]. Tao *et al.* [32] proposed a GP model to model the hysteresis of pneumatic end-effectors. Unfortunately, it is computationally expensive for large datasets due to its $O(N^3)$ complexity. A parametric GP regression (PGPR) method has been proven to able to deal with large datasets [33]. Therefore, whether the PGPR-based method is able to model the hysteresis can be further studied.

Another research point about the elastic torque sensor is the safety. After the maximum deformation of the elastic element, an excessive human–machine interaction torque can be generated due to controller malfunction or external impacts caused by collision. To achieve the human–machine interaction safety, a possible solution is to introduce a clutch in the design of the torque sensors. A clutch is defined as a device that disengages and engages two bodies of the clutch [34], and it can control the human–machine interaction force not to exceed the safety threshold. Woo *et al.* [10] designed a compact rotary torque sensor with a mechanical clutch that automatically disengages transmission when its threshold is reached. The threshold value can be adjusted by a linear compression spring [10]. Zhang and Huang [35] designed an elastic torque sensor with a mechanical clutch that automatically disconnects the transmission between the exoskeleton and the human through an additional motor. However, an additional motor or linear compression spring may make the system heavy and cumbersome. Therefore, how to design a miniaturized clutched elastic torque sensor needs to be further studied.

In this article, a novel elastomer-based clutched torque sensor for hand exoskeleton robots is proposed. An improved PGPR model with a combined kernel function based on the NARMAX structure is established to model hysteresis characteristics. The contributions of this article can be summarized as follows.

1) An elastomer-based torque sensor is developed to achieve miniaturization and lightness. Compared with the state-of-the-art elastic torque sensors for hand exoskeletons, the volume-to-torque ratio of the proposed torque sensor is reduced by 15.48%, and its weight is reduced by 23.33%.
2) A wafer disk clutch is integrated into the torque sensor, and it can limit the torque between the motor and the output end. The force caused by collision on the torque sensor with the clutch can be reduced by 51.78% compared with that of the torque sensor without the clutch.
3) An improved PGPR model with a combined kernel function based on NARMAX structure is proposed to achieve accurate torque sensing, and the root mean squared modeling error (RSME) is less than 1.86%. By comparisons with other intelligent hysteresis modeling results (the maximum absolute error (MAE) is 12.32%), the MAE of the proposed modeling method can be reduced to 7%.

The rest of this article is organized as follows. In Section II, the elastomer-based clutched torque sensor is introduced, and the hysteresis characteristics of the rubber spring are investigated. Section III presents the improved PGPR modeling method for the proposed torque sensor. In Section IV, experimental verifications are conducted. Section V gives the conclusion and future work.

II. Mechanism Design and Hysteresis Phenomenon

A. Overall Design

As shown in Fig. 1, an elastomer-based clutched torque sensor has been designed. The torque sensor uses a ring-shaped rubber spring instead of metal springs, which makes it miniaturized and lightweight. A wafer disk clutch is connected in series between the input end and the rubber spring to limit the transmissible torque. Its dimension is 29.5 mm × 18 mm × 24 mm, and its weight is 23 g. Its maximum measured torque can be up to 0.5 Nm. Table I shows the comparison of the proposed sensor and some existing torque sensors applied to hand exoskeleton robots. Compared with these state-of-the-art torque sensors, the volume-to-torque ratio of the proposed sensor can be reduced by 15.48%, and its weight is reduced by 23.33%. The force caused by collision on the torque sensor with the clutch can be reduced by 51.78% compared with that of the torque sensor without the clutch. In addition to

TABLE I
PROPERTY COMPARISONS BETWEEN THE PROPOSED TORQUE SENSOR AND SOME EXISTING TORQUE SENSORS

Torque sensor	Spring type	Weight (g)	Size (mm)	Maximum measured torque (Nm)	Volume-to-torque ratio	Torque limit
Jo *et al.*	Linear compression	30	18×77×36	Force: 9N	-	×
Agarwal *et al.*[1]	Linear compression	30	44×36×17	0.5	53.86	×
Agarwal *et al.*[2]	Helical torsion	40	38×38×24	0.3	115.52	×
Baldoni *et al.*[3]	Linear compression	-	diameter: 17; length: 28	0.2	31.78	×
Baldoni *et al.*[4]	Linear compression	-	diameter: 16; length: 30	0.2	30.16	×
Refour *et al.*	Linear compression	-	-	Force: 49.41N	-	×
Guo *et al.*	Wave spring	-	56×19×19	Force: 40N	-	×
Bianchi *et al.*	Structural spring	-	-	0.99	-	×
Proposed sensor	Rubber spring	23	29.5×18×24	0.5	25.49	√(↓ 51.78%[5])

[1] and [2] represent the LC-sensor and the HT-sensor in [9], respectively; [3] and [4] represent the first sensor and the second sensor in [8], respectively; [5] represents the comparison of the forces generated by collision on the torque sensor with and without the clutch, which is presented in Section IV-B.

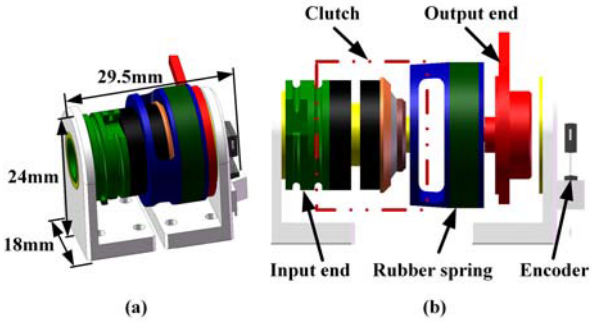

Fig. 1. Dimension and mechanical structure of the proposed elastomer-based clutched torque sensor. (a) Critical dimension. (b) Overall mechanical design.

Fig. 2. Prototype of the proposed elastomer-based clutched torque sensor.

the rubber spring and the clutch, the torque sensor is mainly composed of the input end, the output end, and an encoder. The angle encoder is located on the side of the output end to measure the position of the output end. The input end is connected with a motor by a cable-driven mechanism for actuation applications, and its position can be measured by an angle encoder placed at the end of the motor. The angle measurement error caused by the elongation of the steel cable is negligible since it is tiny. By subtracting the input position from the output position, the angle deformation of the rubber spring can be calculated, and the output torque of the torque sensor can be estimated. The elastomer-based clutched torque sensor prototype has been fabricated based on the CAD model, which is shown in Fig. 2.

The principle of the proposed torque sensor is described in Fig. 3. Fig. 3(a) shows that the clutch and the output end remain stationary when the input end does not rotate. The

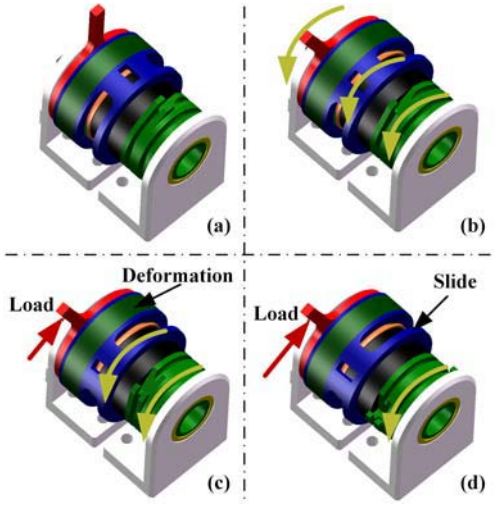

Fig. 3. Principle of the elastomer-based clutched torque sensor. (a) Staticstate. (b) No-loadstate. (c) Load is less than the transmissible torque. (d) Load is greater than the transmissible torque.

measured output torque of the torque sensor is zero. As shown in Fig. 3(b), the input end, the clutch, and the output end rotate counterclockwise simultaneously when the input end rotates but no load is applied to the output end. The measured output torque of the torque sensor is still zero. The input end and the clutch still rotate counterclockwise when a load (the measured output torque) less than the transmissible torque of the clutch is applied to the output end, which is shown in Fig. 3(c). It is worth noting that in this case, the rubber spring deforms, and the torque generated by the deformation reflects the load. Fig. 3(d) shows that only the input end rotates counterclockwise (the motor rotates continuously) when the load is greater than the transmissible torque, and the stator and the rotor of the clutch slide relative to each other. The measured output torque of the torque sensor represents the transmissible torque of the clutch.

B. Rubber Spring Design

A 3-D model of the ring-shaped rubber spring is shown in Fig. 4. The output torque of the rubber spring can be estimated by its torsion deformation. The dimension parameters of the

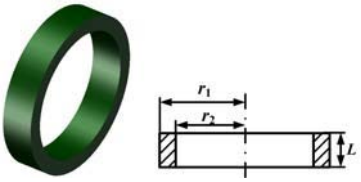

Fig. 4. Diagram of the axonometric and sectioned views of the rubber spring.

rubber spring should be chosen reasonably to avoid fatigue failure and high encumbrance. Therefore, an optimization design approach is proposed and explained as follows.

The material of the rubber spring should be determined first, and the selection is natural rubber. The stiffness of the rubber spring should meet the maximum output torque $T_{\max} = 0.5$ Nm and the maximum angle deformation $\theta_{\max} = 15°$ requirements, and it is expressed as

$$\frac{\pi G\left({r_1}^4 - {r_2}^4\right)}{2L} = \frac{T_{\max}}{\theta_{\max}} \tag{1}$$

where L is the length of the rubber spring, r_1 and r_2 are the outer and inner radii of the rubber spring, respectively. G is the shear modulus of the rubber spring, and $G = 0.117\ e^{0.034\mathrm{HS}}$, where HS stands for the shore hardness of the rubber spring, and it is predetermined here (HS $= 60°$). To avoid fatigue failure, the stress of the rubber spring under the maximum output torque should be less than its required torsional stress $[\sigma] = 0.7$ MPa, which can be expressed as

$$\frac{2T_{\max} r_1}{\pi\left({r_1}^4 - {r_2}^4\right)} \le [\sigma]. \tag{2}$$

The constraints on the length, outer, and inner radii of the rubber spring can be expressed as

$$\begin{cases} L_{\mathrm{lb}} \le L \le L_{\mathrm{ub}} \\ r_{\mathrm{lb}} \le r_2 \le r_1 \le r_{\mathrm{ub}} \end{cases} \tag{3}$$

where $L_{\mathrm{ub}} = 4$ mm and $L_{\mathrm{lb}} = 10$ mm stand for the upper and lower bounds of the length, respectively, and $r_{\mathrm{lb}} = 0$ mm and $r_{\mathrm{ub}} = 10$ mm represent the upper and lower bounds of the outer and inner radii, respectively.

Since the proposed sensor is designed for the hand exoskeleton, the dimension characteristic and the output torque performance of the proposed torque sensor can be evaluated by the volume-to-torque ratio. Its length should also be reasonably selected to suit the width of the finger. Therefore, the nonlinear optimization problem is formulated as follows:

$$\begin{aligned} &\min\ f_{(r_1,r_2,L)} = \frac{a\pi\left({r_1}^2 - {r_2}^2\right)L}{T_{\max}} + bL \\ &\text{s.t. (1), (2) and (3)} \end{aligned} \tag{4}$$

where $a = 0.8$ and $b = 0.2$ represent the weight factors of the volume-to-torque ratio and the length in the design of the rubber spring, respectively. The local optimal solutions have been searched using MATLAB's fmincon function. The length, outer, and inner radii of the rubber spring are finally determined to be 4, 10, and 8.2 mm, respectively.

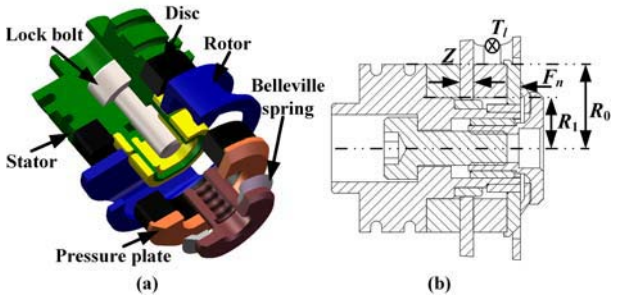

Fig. 5. Clutch design. (a) Mechanical design of the clutch. (b) Schematic of the clutch.

C. Clutch Design

A wafer disk clutch has been proposed and designed to improve the human–machine interaction safety. Fig. 5(a) shows the mechanical structure of the wafer disk clutch. A lock bolt can deform a Belleville spring by tightening, and the Belleville spring can provide a driving force to a pressure plate. The pressure plate is used to compress two thin disks that are coupled to the rotor and the stator of the torque limiter. The transmissible torque between the rotor and the stator is the sum of the residual static friction torque and the active clutching torque [36]. However, the residual static friction torque is ignored here because only few numbers of disks are coupled together. The transmissible torque is determined by some design variables, which are shown in Fig. 5(b). The relationship of the transmissible torque and the design variables can be expressed as

$$T_l = \frac{2\mu Z F_n\left({R_0}^3 - {R_1}^3\right)}{3\left({R_0}^2 - {R_1}^2\right)} \tag{5}$$

where $R_0 = 7.5$ mm and $R_1 = 4.5$ mm represent the outer and inner radii of the thin disks, respectively. $\mu = 0.2$ is the coefficient of friction between the rotor and two thin disks, and $Z = 2$ represents the number of the disk interfaces. F_n stands for the normal force applied between the rotor and the two thin disks, and it can be provided by a Belleville spring. The normal force can be changed by changing the deformation of the Belleville spring, and then the maximum transmissible torque can be changed. To achieve the maximum transmissible torque of 0.5 Nm, the normal force should be 204 N. A Belleville washer (Lee Spring M00620-0060-01200-C) has been chosen, and its calculated load at the flat is 699 N.

D. Testing Rig

A testing rig for the proposed torque sensor has been designed and fabricated to collect data for identifying the hysteresis characteristics of the rubber spring, which is shown in Fig. 6. A Faulhaber motor (Faulhaber 2250S012BX4 with incremental encoder IE3-1024, 51:1 planetary gearhead) is used as the motion source. Its displacement can be transmitted to the input end through a cable-driven mechanism (the material of steel cable: 304 stainless steel, the diameter of steel cable: 0.8 mm), and it is controlled by a

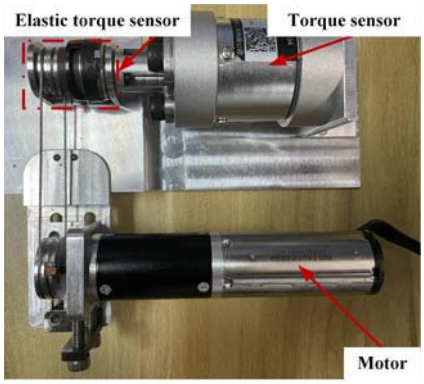

Fig. 6. Testing rig for the proposed torque sensor.

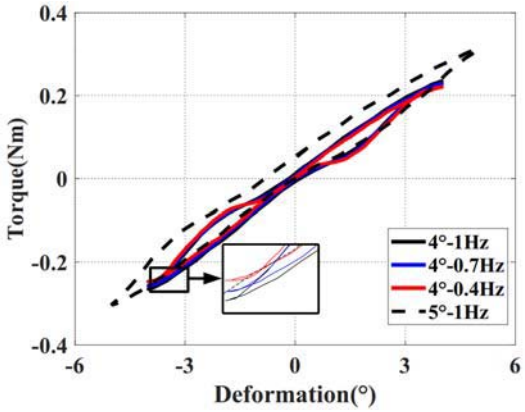

Fig. 7. Hysteresis characteristics of the proposed elastomer-based clutched torque sensor.

motion controller (MCBL3002S, Faulhaber). A torque sensor (DYJN-104, Freud) is used to measure the output torque of the rubber spring, and it is tightly connected to the output end. The deformation of the rubber spring can be directly obtained according to the position sensor placed at the end of the motor. In addition, a DSpace (MicroLabBox RTI1202) is used to exchange position data with the motion controller, and it is also connected with the torque sensor for reading the output torque. The deformation and output torque data of the rubber spring are uploaded and stored on a personal computer.

E. Hysteresis Characteristics and Training Dataset

Different excitation sinusoidal signals are used to investigate the characteristics of the rubber spring. The frequencies of the sinusoidal signals are 0.4, 0.7, and 1 Hz, respectively, and their amplitudes are 4° and 5°, respectively. Fig. 7 shows the torque–deformation curves under signals of different frequencies and amplitudes. The important feature of the curves is that their shapes change with the frequency and amplitude. Therefore, a force sensor model that takes both the frequency-dependent and amplitude-dependent characteristics into account should be designed to achieve accurate torque sensing. To model the hysteresis characteristics and calibrate the proposed torque sensor, more comprehensive excitation sinusoidal signals are used to collect the training data. The frequencies of the sinusoidal signals are 0–1 Hz with an increment of 0.05 Hz, and their amplitudes are 4°–9° with an increment of 0.5°. The hardware constraints of the testing rig determine the upper bounds on the frequency and amplitude.

III. Sensor Model

A. Hysteresis Model

The NARMAX model can predict the current output in terms of past inputs and outputs. It has a strong approximation ability and is an effective method for modeling nonlinear systems [29]. Therefore, the NARMAX model is applied to describe the hysteresis characteristics of the rubber spring, and it can be expressed as

$$y_j = f(x_j) \tag{6}$$

where $x_j = [y_{j-1}, \ldots, y_{j-n_y+1}, u_j, \ldots, u_{j-n_u+1}] \in \mathbb{R}^{n_y+n_u-1}$, $y_j \in \mathbb{R}$ stands for the predicted output torque at the current time instant j, and u_j represents the deformation at the current time instant j. n_y and n_u denote the orders of the output and input variables, respectively. $f(\cdot)$ stands for a nonlinear mapping between the model's input and output variables.

According to the NARMAX model, the training dataset of input–output pairs can be determined as $D = \{\boldsymbol{X}, \boldsymbol{y}\} = \{x_j, y_j\}_{j=1}^{H}$, where H represents the number of the training data, which is approximately 40 000. Therefore, the training dataset D is a sufficiently large dataset to consider the frequency-dependent and amplitude-dependent characteristics. The PGPR method has been proven to have a good ability of using a series of basic Gaussian functions to approximate large dataset. Therefore, an improved PGPR method is used to realize nonlinear mapping $f(\cdot)$ representing the training dataset D in (6).

B. Improved Parametric Gaussian Process Regression

The improved PGPR model includes two GPs: a classical GP and a parametric GP. The classical GP is used to implement $f(\cdot)$ in (6) by conditioning on a hypothetical dataset, and the parametric GP is used to update the hypothetical dataset which is defined in the next paragraph.

Here, assume the existence of a hypothetical dataset $\{\boldsymbol{z}, p\}$. $\boldsymbol{z} = \{z^i\}_{i=1}^{M}$ and $p \in \mathbb{R}^M$, where M denotes the number of hypothetical data. The hypothetical data $\boldsymbol{z}^i$ are the center of the ith cluster among M clusters obtained using the k-means clustering algorithm on $\boldsymbol{X}$, and it is invariant throughout the algorithm. p is the following stochastic vector whose mean value and covariance matrix are estimated by the parametric GP described in Section III-B2:

$$p \sim \mathcal{N}(m, S) \tag{7}$$

where $m \in \mathbb{R}^M$ is the mean of p, and $S \in \mathbb{R}^{M \times M}$ denotes the covariance matrix of p.

1) Classical Gaussian Process: According to [33], a GP is defined to describe $f(\cdot)$ in (6). Let x_* be the input of (6). Then the joint distribution of the hypothetical data p and the

predicted output $p_* = f(x_*)$ can be obtained and expressed as

$$\begin{bmatrix} p \\ p_* \end{bmatrix} \sim \mathcal{N}\left(0, \begin{bmatrix} \operatorname{cov}(z^1, z^1) & \cdots & \operatorname{cov}(z^1, z^M) & \operatorname{cov}(z^1, x_*) \\ \vdots & \ddots & \vdots & \vdots \\ \operatorname{cov}(z^M, z^1) & \cdots & \operatorname{cov}(z^M, z^M) & \operatorname{cov}(z^M, x_*) \\ \operatorname{cov}(x_*, z^1) & \cdots & \operatorname{cov}(x_*, z^M) & \operatorname{cov}(x_*, x_*) \end{bmatrix}\right) \triangleq \mathcal{N}\left(0, \begin{bmatrix} K & q(x_*) \\ q^T(x_*) & \operatorname{cov}(x_*, x_*) \end{bmatrix}\right) \tag{8}$$

where $\operatorname{cov}(s, s') \in \mathbb{R}$ $(s, s' \in \{z^1, z^2, \ldots, z^M, x_*\})$ stands for the symmetric covariance function which is defined by the following kernel function:

$$\operatorname{cov}(s, s') = k_{\mathrm{SE}}(s, s')\left[k_{\mathrm{Lin}}(s, s') + k_{\mathrm{Per}}(s, s')k_{\mathrm{RQ}}(s, s')\right] \tag{9}$$

where

$$k_{\mathrm{SE}}(s, s') = \theta_1^2 \exp\left(-\frac{(s - s')^T(s - s')}{2\theta_2^2}\right) \tag{10}$$

$$k_{\mathrm{Lin}}(s, s') = \theta_3^2(s - \theta_4)^T(s' - \theta_4) \tag{11}$$

$$k_{\mathrm{Per}}(s, s') = \theta_5^2\left(-\frac{2}{\theta_6^2}\left(\sin\left(\pi\frac{s - s'}{\theta_7}\right)\right)^T\left(\sin\left(\pi\frac{s - s'}{\theta_7}\right)\right)\right) \tag{12}$$

$$k_{\mathrm{RQ}}(s, s') = \left(1 + \frac{(s - s')^T(s - s')}{2\theta_8\theta_9^2}\right)^{-\theta_8} \tag{13}$$

where $\theta = [\theta_1, \theta_2, \theta_3, \theta_4, \theta_5, \theta_6, \theta_7, \theta_8, \theta_9]^T \in \mathbb{R}^9$ are the hyperparameters of the GP. One contribution of this article is to propose the above combined kernel function which includes some basic kernel functions such as the squared exponential (SE) function, the linear (Lin) function, the periodic (Per) function, and the rational quadratic (RQ) function, while the original PGPR model proposed in [33] only uses one basic kernel function.

Based on the joint Gaussian prior distribution (8), the distribution of p_* on conditioning p is

$$p_* = f(x_*) \mid p \sim \mathcal{N}\big(q(x_*)^T K^{-1} p, \operatorname{cov}(x_*, x_*) - q(x_*)^T K^{-1} q(x_*)\big). \tag{14}$$

Therefore, in practice, $f(\cdot)$ in (6) can be determined by the mean value of p_*. That is,

$$f(x_*) = E(p_*) = q(x_*)^T K^{-1} E(p) = q(x_*)^T K^{-1} m. \tag{15}$$

According to [33], the hyperparameter θ in (9) can be updated by the stochastic gradient descent method. Assume we have a sample (x_n, y_n) from the training set D. Then, by [33], the updating law for θ can be determined as follows:

$$\theta_{n+1} = \theta_n - \frac{\eta}{2\sigma_n^2}\left[-2(y_n - \mu_n)\frac{\partial \mu_n}{\partial \theta_n} + \frac{\partial \Sigma_n}{\partial \theta_n}\right] \tag{16}$$

$$\log(\sigma_{n+1}^2) = \log(\sigma_n^2) + \frac{\eta}{2\sigma_n^2}\left[(y_n - \mu_n)^2 + \Sigma_n\right] - \frac{\eta}{2} \tag{17}$$

where θ_n is the estimation of θ at the nth updating step, $\eta > 0$ is the learning rate, σ_n is the estimation of the unmodeled part, and

$$\mu_n = q^T(x_n, \theta_n)K^{-1}(\theta_n)m_n \tag{18}$$

$$\Sigma_n = \operatorname{cov}(x_n, x_n, \theta_n) - q^T(x_n, \theta_n)K^{-1}(\theta_n)q(x_n, \theta_n) + q^T(x_n, \theta_n)K^{-1}(\theta_n)S_nK^{-1}(\theta_n)q^T(x_n, \theta_n) \tag{19}$$

where $q(\cdot, \theta_n)$, $\operatorname{cov}(\cdot, \cdot, \theta_n)$ and $K(\theta_n)$ are defined in (8) with θ being θ_n. m_n and S_n denote the estimations of m and S in (7) at the nth updating step, respectively.

2) Parametric Gaussian Process: According to [33], the parametric GP is used to update p_n in the hypothetical dataset. Assume we have a sample (x_n, y_n) from the training set D. Then, by [33], the updating law for the mean value m_n and the covariance matrix S_n can be determined as follows:

$$m_{n+1} = m_n + q^T(x_n, \theta_n)\Sigma_n^{-1}(y_n - \mu_n) \tag{20}$$

$$S_{n+1} = S_n - q^T(x_n, \theta_n)\Sigma_n^{-1}q(x_n, \theta_n). \tag{21}$$

The entire training process of the improved PGPR can be summarized in Algorithm 1.

Algorithm 1 Training Method of the Improved PGPR

1: **Initialize** the cluster number M, the hypothetical data z; $\theta_0 = [ln(0.3), \ldots, ln(0.3)]^T, m_0 = [0, \ldots, 0]^T, S_0 = K(\theta_0), \eta = 0.1, \sigma_0^2 = \frac{\sum(y_j - \bar{y})^2}{H-1}, \bar{y} = \frac{\sum y_j}{H}, H = 4.4554 \times 10^4, n_{\max} = 2 \times 10^5$.
2: **for all** $n \le n_{max}$ **do**
3: Select one sample (x_n, y_n) from the training dataset D;
4: θ_{n+1} is updated by (16), $\log(\sigma_{n+1}^2)$ is updated by (17);
5: m_{n+1} is updated by (18), S_{n+1} is updated by (19);
6: $n \leftarrow n + 1$;
7: **end for**
8: $\theta \leftarrow \theta_n$, $m \leftarrow m_n$, $S \leftarrow S_n$.
9: Given x_*, $f(x_*)$ in (6) can be calculated by $q(x_*)^T K^{-1} m$.

C. Parameters Selection

To accurately estimate the measured value of the torque sensor, the parameters of the proposed sensor model need to be determined. They can be divided into two types: optimized parameters and predetermined parameters. The optimized parameters consist of the hyperparameter θ of the improved PGPR model, and it can be trained by Algorithm 1 on the training dataset D. The predetermined parameters include the orders of the output and the input variables in (6), and the number of the clusters M. They can be manually determined by the trial-and-error method to minimize the following two criteria (the RMSE and the MAE):

$$\mathrm{RMSE} = \sqrt{\frac{1}{Q}\sum_{i=1}^{Q}(y_i - \hat{y}_i)^2} \times 100\% \tag{22}$$

$$\mathrm{MAE} = \max_i |y_i - \hat{y}_i| \times 100\% \tag{23}$$

where $Q = 2 \times 10^3$ is the number of the testing data which are selected from the training dataset D, and y_i and

TABLE II
VALUES OF PARAMETERS IN THE PROPOSED SENSOR MODEL

Parameters	M	n_y	n_u	θ_1	θ_2	θ_3	θ_4	θ_5	θ_6	θ_7	θ_8	θ_9
Value	14	8	8	21.5113	11.8339	-5.4362	-6.5416	-8.7194	5.9948	-2.5506	-5.3729	-5.1467

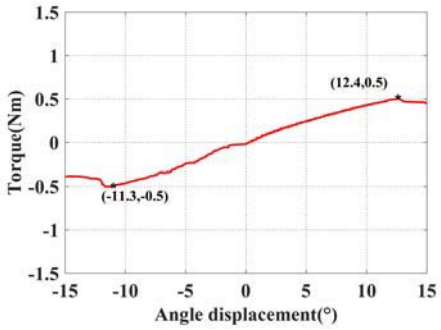

Fig. 8. Measurement results for the angle displacement of the motor and the output torque of the rubber spring at a low speed.

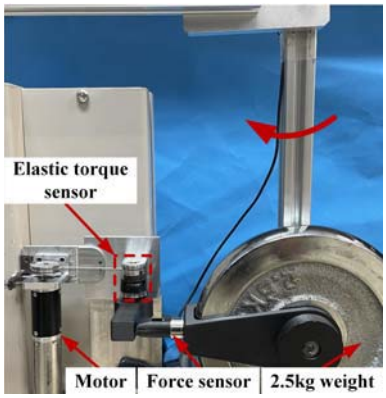

Fig. 9. Testing platform for simulating external impact caused by collision.

$\hat{y}_i$ $(i = 1, \ldots, Q)$ are the actual and the predicted torques, respectively. Here, the predetermined parameters are determined when the RMSE and the MAE on the testing data are 2.83% and 7.67%, respectively.

Using the parameter selection experiment, the parameters of the proposed sensor model have been finally determined and are listed in Table II.

IV. EXPERIMENT

In this section, the experiments are conducted to achieve three objectives: 1) to verify the working principle and the maximum measured torque of the proposed torque sensor; 2) to evaluate the safety performance of the proposed clutched torque sensor, i.e., the magnitude of the force caused by collision; and 3) to assess the measurement performance of the proposed sensor model.

A. Principle Verification

An experiment has been performed to verify the working principle of the proposed torque sensor based on the testing rig described in Section II-D. It is worth noting that the principles described in Fig. 3(a) and (b) are obvious, so only the principles described in Fig. 3(c) and (d) are verified. The motor rotates at a low speed (1 rad/min) in the clockwise (positive direction) and counterclockwise (negative direction) directions from the starting position. The starting position is defined as the position where the deformation of the proposed torque sensor is zero. The angle displacement of the motor and the output torque of the proposed torque sensor are recorded. The angle displacement of the motor can be regarded as the deformation of the rubber spring when the load is within the maximum transmissible torque. The experimental results are shown in Fig. 8. It can be found that the rubber spring deforms below the maximum transmissible torque, and its deformation can reflect the load due to its change in a single direction. When the maximum transmission torque is reached, the stator and the rotor of the clutch slide relatively, which limits the transmission torque. Then the output torque of the rubber spring remains constant at the maximum transmission torque. It is worth noting that the magnitude of the output torque of the torque sensor decreases when the stator and the rotor of the clutch slide relatively, and it is caused by the change from static friction to dynamic friction. In addition, it is observed that the maximum measured output torque of the torque sensor can be approximately up to 0.5 Nm, and the angle deformations in the two directions are 12.4° and −11.3°, respectively. The deformation–torque relationship of the rubber spring is asymmetric, and a similar result is also found in [18].

B. Mechanism Safety

A testing platform simulating external impact caused by collision is designed and fabricated, which is shown in Fig. 9. A dumbbell weighing 2.5 kg is fixed at one end of a link. It can drive the link from the horizontal position to the vertical position. A force sensor (DYZ-100, Freud) is installed in front of the dumbbell to measure the interaction force caused by collision. The torque sensors with and without the clutch are fixed on a base, and their installation position needs to ensure that the dumbbell collides with the torque sensor at the vertical position. To prevent the input end of the torque sensor from moving during collision, the input end is fixed by a motor or other clamping device. The dumbbell is released from the horizontal position, and it collides with the torque sensor at the vertical position. Fig. 10 shows the interaction forces of the torque sensors with and without the clutch, and they are 8.82 and 18.29 N, respectively. Compared with the torque sensor without the clutch, the interaction forces generated on the torque sensor with the clutch can be reduced by 51.78%. Therefore, it is obvious that the torque sensor with the clutch can improve the mechanical safety.

C. Sensor Model Validation

A new validation dataset is collected using a combined excitation sinusoidal signal in the testing rig described in

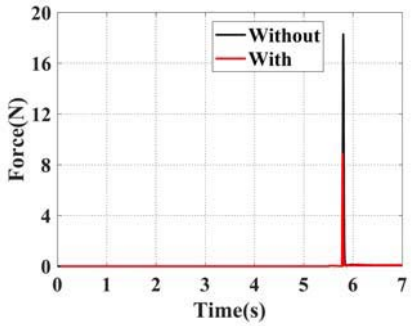

Fig. 10. Comparison of the forces caused by collision on the torque sensors with and without the clutch.

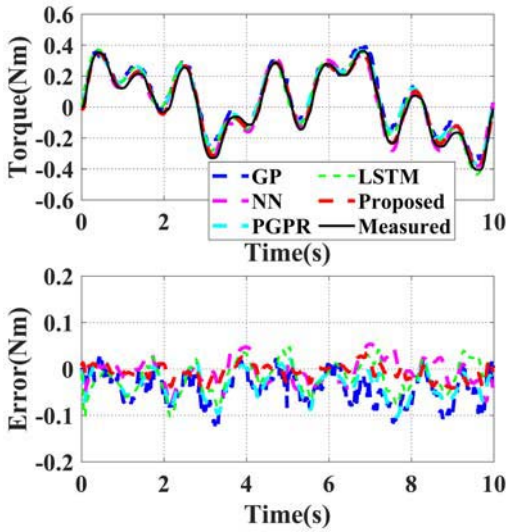

Fig. 11. Sensor modeling performance comparison between the proposed method and some existing methods on the validation dataset.

TABLE III
COMPARISON ON THE ESTIMATION ERROR OF DIFFERENT SENSOR MODELING METHODS

	GP	NN	PGPR	LSTM	Proposed
RMSE	5.26%	2.89%	4.37%	3.71%	1.86%
MAE	12.32%	7.88%	10.38%	10.28%	5.24%

Section II-D. The combined excitation sinusoidal signal can be expressed as

$$h = \sum_{i=1}^{k} A_i \sin 2\pi f_i \tag{24}$$

where k is the number of the sinusoidal functions, and A_i and f_i are the amplitude and frequency of the sinusoidal functions, respectively.

For comparative studies, the NN model, the LSTM model, and the PGPR model proposed in [29], [30], and [33] have been trained using the same training dataset. In addition, the GP model designed in [32] has also been trained by partial data of the training dataset because of hardware limitation. Fig. 11 shows the torque measurement results of the proposed sensor model and the aforementioned models on the validation dataset, and their RMSE and MAE are calculated and given in Table III. The RMSE and MAE of the proposed method are approximately 1.86% and 5.24%, respectively, while the maximum RMSE and MAE of other methods are approximately 5.26% and 12.32%, respectively. Therefore, compared with these existing methods, the proposed method can improve the measurement accuracy of the rubber spring output torque.

V. CONCLUSION

In this article, a novel miniaturized and lightweight elastomer-based clutched torque sensor is proposed for hand exoskeleton robots. A rubber spring is designed and applied to reduce the volume and weight of the torque sensor, and its dimensions are optimized. Compared with the state-of-the-art torque sensors for hand exoskeleton robots, the volume-to-torque ratio of the proposed torque sensor can be reduced by 15.48%, and its weight is reduced by 23.33%. A wafer disk clutch is used to limit the excessive interaction force due to possible external impacts caused by collision. Furthermore, based on the NARMAX structure, the improved PGPR model has been proposed and trained to model the hysteresis nonlinear characteristics in the proposed torque sensor. Finally, the experiments have been conducted to verify the mechanical safety capability and the torque sensing performance. Compared with the torque sensor without the clutch, the interaction force generated on the torque sensor with the clutch can be reduced by 51.78%, which can further improve the mechanical safety. The RSME and MAE of the improved PGPR model on the validation dataset are 1.86% and 5.24%, respectively. The proposed hysteresis model can improve the MAE by up to 7% compared with those of other intelligent hysteresis models. The experimental results indicate that the miniaturized clutched torque sensor can improve the mechanical safety, and ir can achieve an accurate torque sensing based on the proposed sensor model.

In the future, the proposed torque sensor is to be integrated into a hand exoskeleton robot to further verify its performance. Some control methods based on the proposed force sensor model have to be designed and verified to achieve precise force control as well.

REFERENCES

[1] S.-W. Pu, Y.-C. Pei, and J.-Y. Chang, "Decoupling finger joint motion in an exoskeletal hand: A design for robot-assisted rehabilitation," *IEEE Trans. Ind. Electron.*, vol. 67, no. 1, pp. 686–697, Jan. 2020.
[2] D. Wang, Q. Meng, Q. Meng, X. Li, and H. Yu, "Design and development of a portable exoskeleton for hand rehabilitation," *IEEE Trans. Neural Syst. Rehabil. Eng.*, vol. 26, no. 12, pp. 2376–2386, Dec. 2018.
[3] A. U. Pehlivan, F. Sergi, and M. K. O'Malley, "A subject-adaptive controller for wrist robotic rehabilitation," *IEEE/ASME Trans. Mechatronics*, vol. 20, no. 3, pp. 1338–1350, Jun. 2015.
[4] D. Wang, J. Guo, C. Sun, M. Xu, and Y. Zhang, "A flexible concept for designing multiaxis force/torque sensors using force closure theorem," *IEEE Trans. Instrum. Meas.*, vol. 62, no. 7, pp. 1951–1959, Jul. 2013.
[5] K. J. Xu, C. Li, and Z. N. Zhu, "Dynamic modeling and compensation of robot six-axis wrist force/torque sensor," *IEEE Trans. Instrum. Meas.*, vol. 56, no. 5, pp. 2094–2100, Oct. 2007.
[6] F. Zhang, L. Yang, and Y. Fu, "Design of a novel elastic torque sensor for hand injuries rehabilitation based on bowden cable," *IEEE Trans. Instrum. Meas.*, vol. 68, no. 9, pp. 3184–3192, Sep. 2019.
[7] J. Zhou, F. Malric, and S. Shirmohammadi, "A new hand-measurement method to simplify calibration in cyberglove-based virtual rehabilitation," *IEEE Trans. Instrum. Meas.*, vol. 59, no. 10, pp. 2496–2504, Oct. 2010.
[8] A. Baldoni, M. Cempini, M. Cortese, S. Crea, M. C. Carrozza, and N. Vitiello, "Design and validation of a miniaturized SEA transmission system," *Mechatronics*, vol. 49, pp. 149–156, Feb. 2018.

[9] P. Agarwal and A. D. Deshpande, "Series elastic actuators for small-scale robotic applications," *J. Mech. Robot.*, vol. 9, no. 3, Jun. 2017, Art. no. 031016.
[10] H. Woo, B. Na, and K. Kong, "Design of a compact rotary series elastic actuator for improved actuation transparency and mechanical safety," in *Proc. IEEE Int. Conf. Robot. Autom. (ICRA)*, Singapore, May 2017, pp. 1872–1877.
[11] D. Marconi, A. Baldoni, Z. McKinney, M. Cempini, S. Crea, and N. Vitiello, "A novel hand exoskeleton with series elastic actuation for modulated torque transfer," *Mechatronics*, vol. 61, pp. 69–82, Aug. 2019.
[12] I. Jo and J. Bae, "Design and control of a wearable and force-controllable hand exoskeleton system," *Mechatronics*, vol. 41, pp. 90–101, Feb. 2017.
[13] Y. Guo, W. Xu, S. Pradhan, C. Bravo, and P. Ben-Tzvi, "Data driven calibration and control of compact lightweight series elastic actuators for robotic exoskeleton gloves," *IEEE Sensors J.*, vol. 21, no. 19, pp. 21120–21130, Oct. 2021.
[14] P. Agarwal, J. Fox, M. K. O'Malley, A. D. Deshpande, and Y. Yun, "An index finger exoskeleton with series elastic actuation for rehabilitation: Design, control and performance characterization," *Int. J. Robot. Res.*, vol. 34, no. 14, pp. 1747–1772, Oct. 2015.
[15] Y. Yun, P. Agarwal, J. Fox, K. E. Madden, and A. D. Deshpande, "Accurate torque control of finger joints with UT hand exoskeleton through bowden cable SEA," in *Proc. IEEE/RSJ Int. Conf. Intell. Robots Syst. (IROS)*, Daejeon, South Korea, Dec. 2016, pp. 390–397.
[16] E. M. Refour, B. Sebastian, R. J. Chauhan, and P. Ben-Tzvi, "A general purpose robotic hand exoskeleton with series elastic actuation," *J. Mech. Robot.*, vol. 11, no. 6, Dec. 2019, Art. no. 060902.
[17] M. Bianchi *et al.*, "Design of a series elastic transmission for hand exoskeletons," *Mechatronics*, vol. 51, pp. 8–18, May 2018.
[18] D.-H. Kim and J.-H. Oh, "Hysteresis modeling for torque control of an elastomer series elastic actuator," *IEEE/ASME Trans. Mechatronics*, vol. 24, no. 3, pp. 1316–1324, Jun. 2019.
[19] C. Jarrett and A. McDaid, "Modeling and feasibility of an elastomer-based series elastic actuator as a haptic interaction sensor for exoskeleton robotics," *IEEE/ASME Trans. Mechatronics*, vol. 24, no. 3, pp. 1325–1333, Jun. 2019.
[20] D. Chiaradia, L. Tiseni, and A. Frisoli, "Compact series visco-elastic joint (SVEJ) for smooth torque control," *IEEE Trans. Haptics*, vol. 13, no. 1, pp. 226–232, Jan. 2020.
[21] K. Abe, T. Suga, and Y. Fujimoto, "Control of a biped robot driven by elastomer-based series elastic actuator," in *Proc. 12th IEEE Int. Workshop Adv. Motion Control (AMC)*, Sarajevo, Bosnia and Herzegovina, Mar. 2012, pp. 1–6.
[22] S. Takaoka, H. Yamada, and S. Hirose, "Snake-like active wheel robot ACM-R4.1 with joint torque sensor and limiter," in *Proc. IEEE/RSJ Int. Conf. Intell. Robots Syst.*, San Francisco, CA, USA, Sep. 2011, pp. 1081–1086.
[23] J. Austin, A. Schepelmann, and H. Geyer, "Control and evaluation of series elastic actuators with nonlinear rubber springs," in *Proc. IEEE/RSJ Int. Conf. Intell. Robots Syst. (IROS)*, Hamburg, Germany, Dec. 2015, pp. 6563–6568.
[24] J. Paskarbeit, S. Annunziata, D. Basa, and A. Schneider, "A self-contained, elastic joint drive for robotics applications based on a sensorized elastomer coupling—Design and identification," *Sens. Actuators A, Phys.*, vol. 199, pp. 56–66, Sep. 2013.
[25] F. Parietti, G. Baud-Bovy, E. Gatti, R. Riener, L. Guzzella, and H. Vallery, "Series viscoelastic actuators can match human force perception," *IEEE/ASME Trans. Mechatronics*, vol. 16, no. 5, pp. 853–860, Oct. 2011.
[26] A. Schepelmann, K. A. Geberth, and H. Geyer, "Compact nonlinear springs with user defined torque-deflection profiles for series elastic actuators," in *Proc. IEEE Int. Conf. Robot. Autom. (ICRA)*, Hong Kong, Sep. 2014, pp. 3411–3416.
[27] C. Jarrett and A. J. McDaid, "Robust control of a cable-driven soft exoskeleton joint for intrinsic human-robot interaction," *IEEE Trans. Neural Syst. Rehabil. Eng.*, vol. 25, no. 7, pp. 976–986, Jul. 2017.
[28] W. Choi, J. Won, J. Lee, and J. Park, "Low stiffness design and hysteresis compensation torque control of SEA for active exercise rehabilitation robots," *Auton. Robots*, vol. 41, no. 5, pp. 1221–1242, Jun. 2017.
[29] L. Cheng, W. Liu, Z.-G. Hou, J. Yu, and M. Tan, "Neural-network-based nonlinear model predictive control for piezoelectric actuators," *IEEE Trans. Ind. Electron.*, vol. 62, no. 12, pp. 7717–7727, Dec. 2015.
[30] X. Z. Xia and L. Cheng, "Adaptive Takagi-Sugeno fuzzy model and model predictive control of pneumatic artificial muscles," *Sci. China-Technol. Sci.*, vol. 64, no. 10, pp. 7717–7727, 2021.
[31] Y.-D. Tao, H.-X. Li, and L.-M. Zhu, "Hysteresis modeling with frequency-separation-based Gaussian process and its application to sinusoidal scanning for fast imaging of atomic force microscope," *Sens. Actuators A, Phys.*, vol. 311, Aug. 2020, Art. no. 112070.
[32] Y.-D. Tao, H.-X. Li, and L.-M. Zhu, "Rate-dependent hysteresis modeling and compensation of piezoelectric actuators using Gaussian process," *Sens. Actuators A, Phys.*, vol. 295, pp. 357–365, Aug. 2019.
[33] M. Raissi, H. Babaee, and G. E. Karniadakis, "Parametric Gaussian process regression for big data," *Comput. Mech.*, vol. 64, no. 2, pp. 409–416, Aug. 2019.
[34] M. Plooij, G. Mathijssen, P. Cherelle, D. Lefeber, and B. Vanderborght, "Lock your robot: A review of locking devices in robotics," *IEEE Robot. Autom. Mag.*, vol. 22, no. 1, pp. 106–117, Mar. 2015.
[35] T. Zhang and H. Huang, "Design and control of a series elastic actuator with clutch for hip exoskeleton for precise assistive magnitude and timing control and improved mechanical safety," *IEEE/ASME Trans. Mechatronics*, vol. 24, no. 5, pp. 2215–2226, Oct. 2019.
[36] M. R. Tucker, C. Shirota, O. Lambercy, J. S. Sulzer, and R. Gassert, "Design and characterization of an exoskeleton for perturbing the knee during gait," *IEEE Trans. Biomed. Eng.*, vol. 64, no. 10, pp. 2331–2343, Oct. 2017.

Ning Sun received the B.E. degree in mechanical engineering from Qingdao University, Qingdao, China, in 2015, and the M.S. degree in mechanical engineering from the Beijing Institute of Technology, Beijing, China, in 2018. He is currently pursuing the Ph.D. degree in control theory and control engineering with the State Key Laboratory of Management and Control for Complex Systems, Institute of Automation, Chinese Academy of Sciences, Beijing.

His current research interests include rehabilitation robot design and compliant actuator technology.

Long Cheng (Senior Member, IEEE) received the B.S. degree (Hons.) in control engineering from Nankai University, Tianjin, China, in 2004, and the Ph.D. degree (Hons.) in control theory and control engineering from the Institute of Automation, Chinese Academy of Sciences, Beijing, China, in 2009.

He is currently a Full Professor with the Institute of Automation, Chinese Academy of Sciences. He is also an Adjunct Professor with the University of Chinese Academy of Sciences, Beijing. He has authored or coauthored more than 100 technical articles in peer-refereed journals and prestigious conference proceedings. His research interests include rehabilitation robot, intelligent control, and neural networks.

Dr. Cheng was a recipient of the IEEE TRANSACTIONS ON NEURAL NETWORKS Outstanding Paper Award from the IEEE Computational Intelligence Society, the Aharon Katzir Young Investigator Award from the International Neural Networks Society, and the Young Researcher Award from the Asian–Pacific Neural Networks Society. He is currently an Associate Editor/Editorial Board Member of IEEE TRANSACTIONS ON CYBERNETICS, IEEE TRANSACTIONS ON AUTOMATION SCIENCE AND ENGINEERING, *Neural Processing Letters*, *Neurocomputing*, *International Journal of Systems Science*, and *Acta Automatica Sinica*.

Xiuze Xia received the B.E. degree in control engineering from the Beijing Institute of Technology, Beijing, China, in 2020. He is currently pursuing the Ph.D. degree in control theory and control engineering with the State Key Laboratory of Management and Control Complex Systems, Institute of Automation, Chinese Academy of Sciences, Beijing.

His research interests include rehabilitation robots and human–robot interaction control.